

# High- $T_C$ Interfacial Ferromagnetism in $\text{SrMnO}_3/\text{LaMnO}_3$ Superlattices

Marius Keunecke, Fryderyk Lyzwa, Danny Schwarzbach, Vladimir Roddatis,  
Nicolas Gauquelin, Knut Müller-Caspary, Johann Verbeeck, Sara J. Callori,  
Frank Klose, Markus Jungbauer, and Vasily Moshnyaga\*

**Heterostructures of strongly correlated oxides demonstrate various intriguing and potentially useful interfacial phenomena.  $\text{LaMnO}_3/\text{SrMnO}_3$  superlattices are presented showcasing a new high-temperature ferromagnetic phase with Curie temperature,  $T_C \approx 360$  K, caused by electron transfer from the surface of the  $\text{LaMnO}_3$  donor layer into the neighboring  $\text{SrMnO}_3$  acceptor layer. As a result, the  $\text{SrMnO}_3$  (top)/ $\text{LaMnO}_3$  (bottom) interface shows an enhancement of the magnetization as depth-profiled by polarized neutron reflectometry. The length scale of charge transfer,  $\lambda_{TF} \approx 2$  unit cells, is obtained from in situ growth monitoring by optical ellipsometry, supported by optical simulations, and further confirmed by high resolution electron microscopy and spectroscopy. A model of the inhomogeneous distribution of electron density in  $\text{LaMnO}_3/\text{SrMnO}_3$  layers along the growth direction is concluded to account for a complex interplay between ferromagnetic and antiferromagnetic layers in superlattices.**

## 1. Introduction

Perovskite heterostructures provide a rich playing field to design and engineer oxide interfaces with the final goal of searching for interfacial “emergent phases” (EP)<sup>[1]</sup> with unusual electronic behavior. The EPs possess electric and magnetic properties which strongly differ from the properties of the constituent layers. Prominent examples include: a) a metallic phase between insulating  $\text{LaAlO}_3$  (LAO) and  $\text{SrTiO}_3$  (STO);<sup>[2]</sup> b) a ferromagnetic

metallic (FMM) phase<sup>[3]</sup> between two anti-ferromagnetic insulators (AFMI)  $\text{LaMnO}_3/\text{SrMnO}_3$  (LMO/SMO); c) FMM phase between the AFMI and a paramagnetic metallic (PMM) manganites;<sup>[4]</sup> d) a superconducting phase between the AFMI and PMM cuprates.<sup>[5]</sup> The formation of interfacial EPs could be controlled by the purposeful change of control parameters, e.g., hole doping, across the interface according to the bulk phase diagram of the constituent materials.<sup>[3,4]</sup> Moreover, the EPs can also be created by deliberate engineering of interfaces, yielding the optimization of electronic<sup>[6]</sup> and/or structural<sup>[7]</sup> properties of heterostructures by insertion of 1–2 additional unit cells (u.c.), e.g.,  $\text{CaRuO}_3$  or  $\text{LaMnO}_3$ , after the manganite (LCMO) layer, or 1 u.c. of  $\text{La}_{1-x}\text{Sr}_x\text{MnO}_3$  (LSMO) layer in between LAO and STO<sup>[8]</sup> or a double Sr-O layers at the LSMO/STO interface.<sup>[9]</sup> In some cases, like a) and c), a direct analogy with the bulk phase diagram is not so evident or still missing.<sup>[2,4]</sup> Nevertheless, in all cases, the properties of EPs, are confined within a very narrow interfacial region of 1–2 u.c. and the EP thickness does not depend on the thickness of the constituting layers.

Digital  $(\text{LMO})_m/(\text{SMO})_n$  superlattices (SLs) with integer number ( $m, n$ ) of unit cells are artificial layered systems, in

M. Keunecke, Dr. M. Jungbauer, Prof. V. Moshnyaga  
Erstes Physikalisches Institut  
Georg-August-Universität-Göttingen  
Friedrich-Hund-Platz 1, 37077 Göttingen, Germany  
E-mail: vmosnea@gwdg.de

F. Lyzwa  
Department of Physics and Fribourg Center for Nanomaterials  
University of Fribourg  
Chemin du Musée 3, CH-1700 Fribourg, Switzerland  
D. Schwarzbach, Dr. V. Roddatis  
Institut für Materialphysik  
Georg-August-Universität-Göttingen  
Friedrich-Hund-Platz 1, 37077 Göttingen, Germany

 The ORCID identification number(s) for the author(s) of this article can be found under <https://doi.org/10.1002/adfm.201808270>.

<sup>[+]</sup>Present address: Forschungszentrum Jülich; Physics of Nanoscale Systems (ER-C-1), Wilhelm-Johnen-Straße, 52425 Jülich, Germany

Dr. N. Gauquelin, Dr. K. Müller-Caspary,<sup>[+]</sup> Prof. J. Verbeeck  
EMAT  
University of Antwerp  
Groenenborgerlaan 171, 2020 Antwerp, Belgium  
Dr. S. J. Callori, Prof. F. Klose  
Australian Centre for Neutron Scattering  
ANSTO  
New Illawarra Road, Lucas Heights, NSW 2234, Australia  
Dr. S. J. Callori  
Department of Physics  
California State University  
San Bernardino, CA 92407, USA  
Prof. F. Klose  
Guangdong Technion-Israel Institute of Technology 241  
Da Xue Road Shantou 515063, P. R. China

which the temperature of the metal–insulator transition,  $T_{MI}$ , was found to critically depend on the  $m/n$  ratio.<sup>[10–16]</sup> The layered architecture allows one to diminish the A-site disorder while keeping the averaged Sr-doping,  $x = n/(m + n)$ , close to the optimal level, i.e.,  $x = 1/4$  or  $1/3$ , for  $m = 3n$  or  $m = 2n$ , respectively. The LMO and SMO layers represent parent compounds of a prototypic double exchange manganite LSMO, in which a random distribution of Sr ions over A-sites results in an FMM ground state with the highest  $T_C \approx 370$  K, observed in bulk LSMO with  $x = 1/3$ . Stoichiometric bulk LMO and SMO are known as A- and G-type antiferromagnets (AFM), respectively, with the Neel temperatures of  $T_N = 140$  K (LMO) and  $T_N = 233\text{--}260$  K (SMO).<sup>[17,18]</sup> The SLs, usually grown by pulsed laser deposition (PLD) and molecular beam epitaxy (MBE), display electrical and magnetic behavior of bulk LSMO<sup>[19]</sup> for very thin LMO and SMO layers,  $n = 1\text{--}2$  u.c., whereas for thicker layers,  $n \geq 3$ , an insulating ground state is observed. Moreover, an interfacial FM emergent phase with Curie temperature,  $T_C \approx 100\text{--}180$  K, has been detected by polarized neutron scattering<sup>[3,16]</sup> and assigned to the atomically sharp LMO/SMO interface. The reverse interface, i.e., SMO/LMO was found to be rather rough and not contributing to the magnetic signal.<sup>[20]</sup>

It is believed that the EP formation is related to interfacial charge transfer.<sup>[5,21]</sup> Some indications for electronic/orbital reconstruction at the LMO/SMO interfaces have been revealed by resonant soft X-ray scattering<sup>[15]</sup> and linear/circular magnetic dichroism at the Mn L<sub>2,3</sub>-edge,<sup>[13]</sup> yielding the estimated charge leakage length  $\approx 1\text{--}3$  u.c. The driving force for charge transfer, i.e., electrostatic (polar) mismatch<sup>[2,22]</sup> with accompanying interfacial orbital/spin reconstructions,<sup>[23,24]</sup> could be influenced by substrate-lattice mismatch, temperature, oxygen partial pressure, etc. Hence, the growth conditions might play an important role in the interfacial charge transfer as well as in the EP formation. Moreover, it would be tempting to probe *in situ* the evolution of the thickness and charge density within the layers at the submonolayer scale during the growth.

Here we report a novel high- $T_C$  FM phase in LMO/SMO SLs grown by a metalorganic aerosol deposition (MAD) technique<sup>[25,26]</sup> at high oxygen partial pressure,  $p_{O_2} \approx 0.2$  bar, allowing *an in situ* growth monitoring by optical ellipsometry. Surprisingly, a complex two-phase magnetic behavior with low-(LTP) and high-temperature (HTP) FM phases with  $T_{C1} \approx 160\text{--}270$  K and  $T_{C2} \approx 360$  K, respectively, was observed. The HTP forms at/close to the SMO/LMO interface because of charge transfer from the electron-rich LMO to the electron-poor SMO layers at a characteristic length scale,  $\lambda_{TF} \approx 2$  u.c., as shown by the Figure in the table of contents, which schematically presents the main experimental results. An interplay of AFM and FM interactions, caused by electronic and orbital reconstructions, governed by the growth procedure and SL design, is discussed.

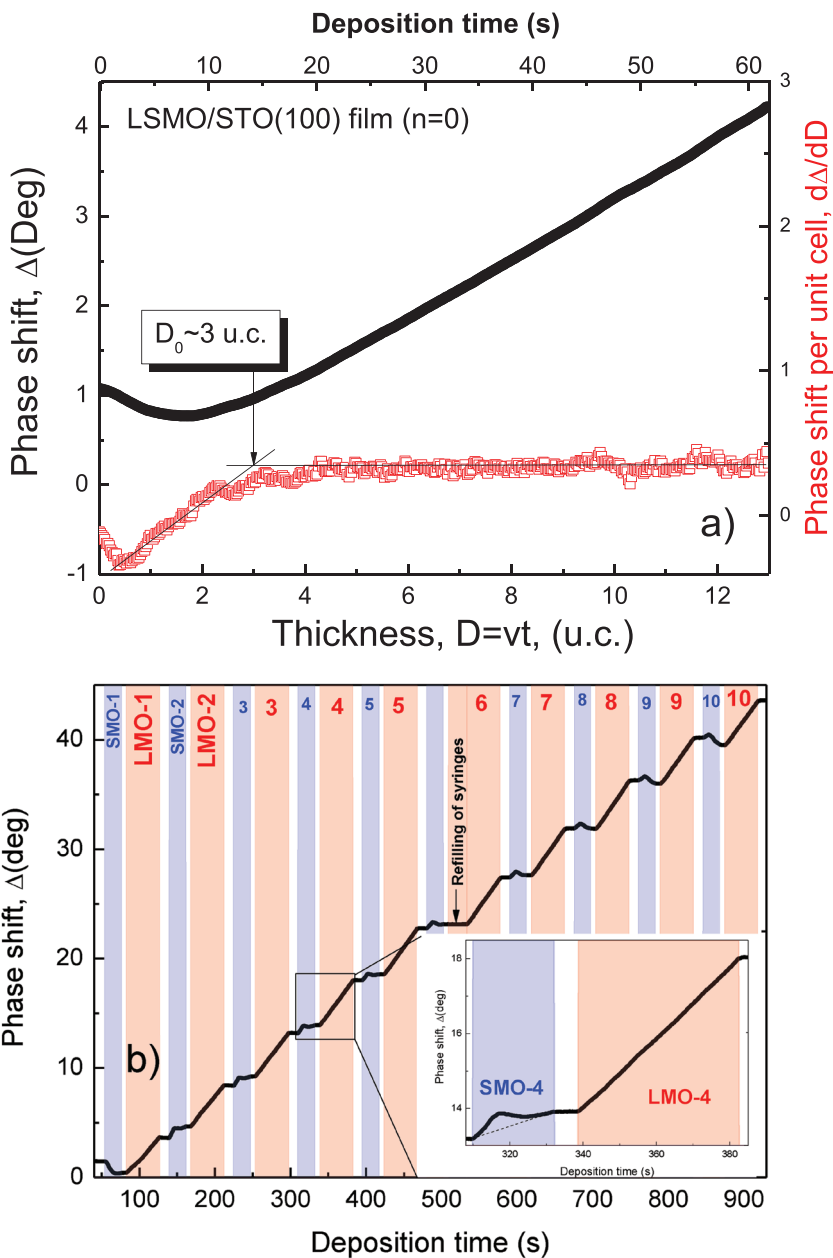
## 2. Results and Discussion

Figure 1 displays the *in situ* monitoring of the ellipsometric phase shift angle,  $\Delta(t)$ , during the growth of a single LSMO/STO(100) film and of an SL sample of LMO<sub>15</sub>/SMO<sub>5</sub> ( $n = 5$ ), which is in the focus of this study. After the first 10–13 s of

growth the phase shift angle,  $\Delta$ , increases almost linearly with time, yielding a constant phase shift rate,  $A = d\Delta/dt \approx 0.08^\circ \text{ s}^{-1}$ , and illustrating a linear relation between the film thickness,  $D$ , and deposition time,  $t$ , i.e., a constant growth rate of the film,  $v = D/t$ , provided by the constant supply rate of the precursor solution. Hence, the parameter  $A$ , which also reflects the electronic properties of the LSMO film (will be discussed below), was taken as a measure of the film thickness. The minimum in  $\Delta(t)$  around the first  $\approx 10$  s of LSMO growth or thickness,  $D_0 \approx 3$  u.c. (see Figure 1a), is characteristic for all MAD-grown film samples. It is related to the initial growth stage at the LSMO/STO interface, dominated by the formation of 2D islands<sup>[27]</sup> with a reduced mobility, resulting in a decrease of  $\Delta$  due to a not fully covered surface. After overcoming this region, the growth is changed into a “step-flow” mode and finalizes in an atomically smooth surface with a mean-square roughness,  $\sigma_{\text{surface}} \approx 0.2$  nm, as evidenced by scanning tunneling microscopy (STM) (see Figure S1 in the Supporting Information).

The growth of the LMO/SMO SL with  $n = 5$  (see Figure 1b) starts with 5 u.c. of SMO, followed by sequential deposition of the LMO<sub>15</sub>/SMO<sub>5</sub>/LMO<sub>15</sub>/... layers with a total number of bilayers,  $K = 10$ . All deposition processes are controlled by pulses of SMO and LMO precursor flux, marked by “blue” (SMO) and “red” (LMO) colors in Figure 1b. The resulting  $\Delta(t)$  increases linearly within the LMO layers, reflecting an increase of the layer thickness similar to what was observed during the LSMO growth (see Figure 1a). In contrast, the SMO reveals a complex growth behavior with initial fast increase in  $\Delta(t)$ , followed by slowing it down (see the inset in Figure 1b). Note that during the pauses between the LMO and SMO pulses the signal  $\Delta(t)$  stays constant, indicating no changes in the optical properties of the already grown LMO and SMO layers.

The *ex situ* X-ray diffraction (XRD) and X-ray reflectometry (XRR) structural characterization (see Figure 2) of SL with  $n = 5$  (other SLs with different LMO and SMO thickness,  $n = 1\text{--}5$ , are shown in Figure S2 in the Supporting Information) reveals the designed epitaxial SL growth in agreement with the *in situ* optical data. From the XRR patterns one can clearly see that a chemical modulation due to the alternating LMO and SMO layers persists even for the SL with the thinnest SMO layer, i.e.,  $n = 1$  u.c. (see Figure S2 in the Supporting Information). For  $n > 1$  we simulated the measured XRR curves (see Figure S3 in the Supporting Information) and obtained a good correspondence with an error  $\approx 5\%$  between the nominal bilayer thickness and that measured by XRR (see Table 1). The simulated mean-square-roughness at the LMO/SMO interfaces,  $\sigma_{\text{LMO/SMO}} \approx 0.1$  nm, and at the surface of the SL,  $\sigma_{\text{vac}} \approx 0.1$  nm, were obtained. They are in line with the measured STM surface roughness,  $\sigma = 0.2$  nm (see Figure S1 in the Supporting Information) and with the atomically sharp interfaces visualized by transmission electron microscopy (TEM) (see Figure 3). The out-of-plane *c*-axis lattice constants of LMO and SMO layers were obtained from simulations of the measured XRD patterns (see Figure S4 in the Supporting Information) and summarized in Table 1. By comparing them with the corresponding bulk values<sup>[18,20]</sup> the information on the strain state of individual layers in the SL could be obtained. The simulated *c*-axis of LMO in the  $n = 5$  SL,  $C_{\text{LMO-SL}} = 0.388$  nm, is smaller than that of a bulk LMO ( $C_{\text{bulk}} = 0.393$  nm) and of a single



**Figure 1.** a) The phase shift angle as a function of deposition time,  $\Delta(t)$ , for a single  $\text{LSMO}/\text{STO}(100)$  film with overall thickness,  $D = 5$  nm, reveals a linear increase of  $\Delta$  after overcoming a transition region of  $D_0 \approx 3$  u.c. in agreement with a linear increase of the film thickness at a constant deposition rate,  $v \approx 0.08 \text{ nm s}^{-1} \approx 0.2 \text{ u.c. s}^{-1}$ ; b) the  $\Delta(t)$  curve for the superlattice  $[(\text{LMO}_{15}/\text{SMO}_5)]_{10}$ . The intervals, marked with blue and red color, represent SMO and LMO precursor pulses, respectively, separated by delay time. The zoomed view (inset in (b)) on the fourth (SMO/LMO) bilayer demonstrates a complex  $\Delta(t)$  behavior during the growth of 5 u.c. of SMO and a linear dependence of  $\Delta$  during the growth of an LMO layer.

$\text{LMO}/\text{STO}(100)$  film,  $C_{\text{LMO-Film}} = 0.390 \text{ nm}$ , indicating a small in-plane tensile stress,  $\epsilon \approx 0.5\%$ , in the LMO layers. The relatively small out-of-plane pseudocubic lattice constant of LMO likely infers the absence of in-plane compressive strain in LMO layers in SLs as well as in single LMO/STO films, grown by MAD under strongly oxidizing MAD conditions,  $p\text{O}_2 \approx 0.2 \text{ bar}$ . Moreover, the small  $C$ -values in films are in quantitative agreement with those of bulk LMO samples, having an

excess of oxygen, i.e.,  $\text{LaMnO}_{3+\delta}$ , and rhombohedral ( $R-3c$ ) structure.<sup>[28]</sup> Further, one could suggest that a hole doping in LMO due to  $\delta$ -oxygen and/or small La deficiency, i.e., formation of  $\text{LaMn}^{3+}_{1-x}\text{Mn}^{4+}_x\text{O}_{3+\delta}$ , may lead to metallic conductivity of LMO. However, the resistivity,  $\rho(T)$ , curves (see Figure S5 in the Supporting Information) reveal an insulating behavior both in the SL with  $n = 5$  and single LMO/STO films, indicating that the hole doping (if any) is rather small,  $x = 0-0.05$ . The fitted  $c$ -axis lattice parameter of SMO in the  $n = 5$  SL,  $C_{\text{SMO-SL}} = 0.375 \text{ nm}$ , is significantly reduced compared to the reference bulk value,  $C_{\text{SMO}} = 0.3805 \text{ nm}$ , indicating a significantly larger tensile stress,  $\epsilon \approx 1.4\%$ , in the SMO layers.

The local structural and chemical characterization of the SL with  $n = 5$  and  $K = 30$  is presented in Figure 3. The “high-angle-annular-dark-field” (HAADF)-scanning transmission electron microscopy (STEM) image in Figure 3a) infers that the whole SL consisting of 30 (SMO/LMO) bilayers exactly matches its total designed film thickness of  $D \approx 220 \text{ nm}$ . Moreover, the atomically sharp, flat and structurally similar LMO/SMO and SMO/LMO interfaces are clearly seen in the high resolution HAADF-HRSTEM image on the left of Figure 3c,d. From the intensity profiles of the Sr- and La-atomic columns in electron energy loss spectroscopy (EELS), quantified along the growth direction (see Figure 3b) using a “Voronoi diagram” (see ref. [29]), one can deduce a slightly different width of these interfaces, i.e., a sharp SMO/LMO interface with a width of  $w < 1$  u.c., and a more diffuse ( $w \approx 1-2$  u.c.) LMO/SMO interface in agreement with the HAADF intensity profile presented in Figure S6 in the Supporting Information. This is also reflected in the asymmetry of these interfaces at the O  $k$  edge,  $E = 533-535 \text{ eV}$ , yielding an electronically sharp SMO/LMO and an electronically more diffuse LMO/SMO interface. Our observations are in contrast with the earlier reports on structurally very asymmetric interfaces, i.e., smooth LMO/SMO and rough SMO/LMO, reported by May et al.<sup>[16]</sup> in the MBE-grown SLs. It appears that specific MAD conditions such as relatively high deposition temperature and high  $p\text{O}_2$ , favor a high surface mobility of adatoms and ensure a step-flow growth mode evidenced by STM (see Figure S1 in the Supporting Information).

Details of the electronic structure were revealed by performing electron energy loss near edge structural analysis (ELNES) at the Mn  $L_{2,3}$  and O  $K$  edge, presented in Figure 3c,d, respectively. It can be seen that the O  $K$  edge and Mn  $L$  edge are similar to those in bulk LMO and SMO in the center of

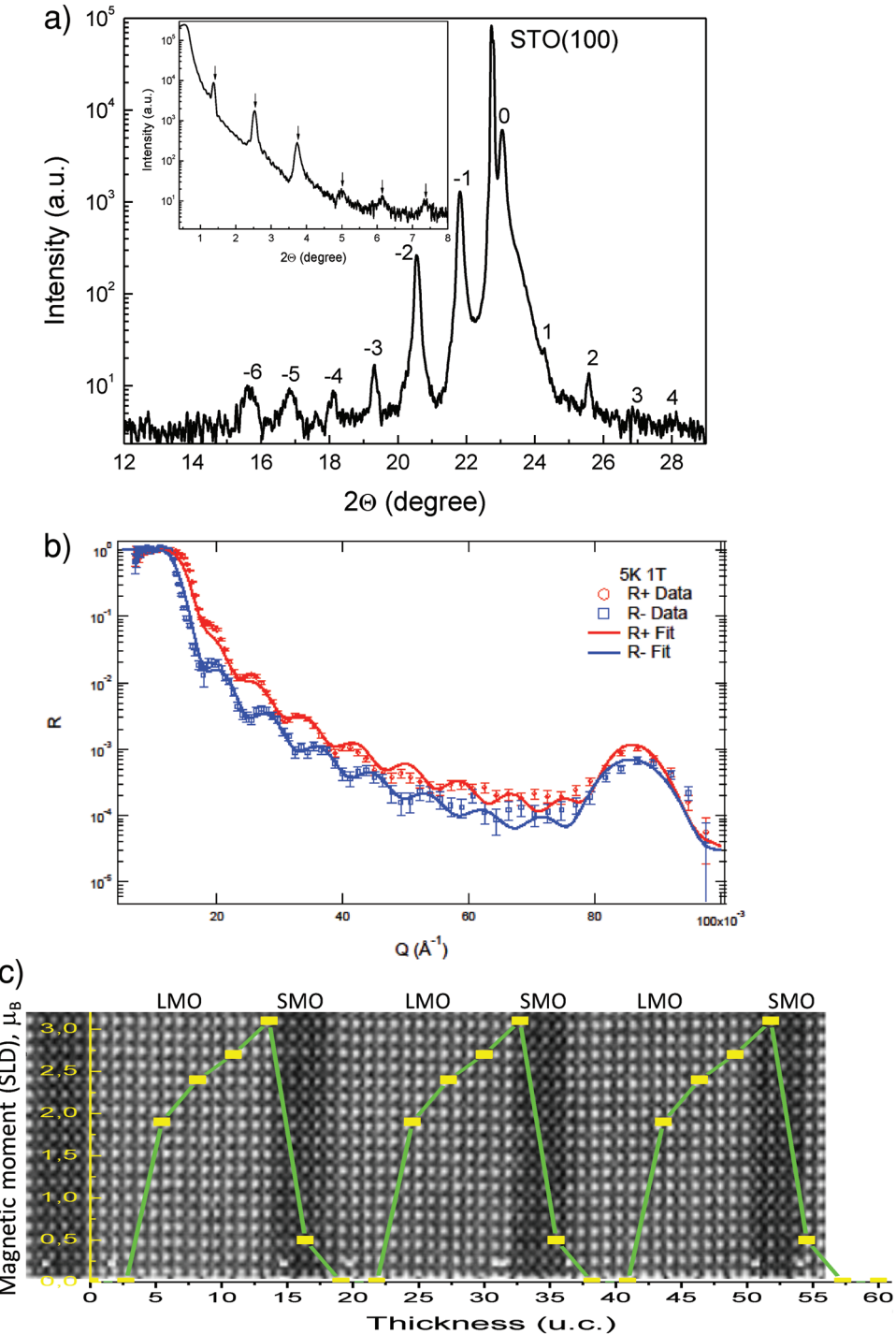


**Figure 2.** a) X-ray diffraction (XRD) around the substrate STO(001) peak and X-ray reflectivity (XRR) of an SL with  $n = 5$ ; b) small-angle polarized neutron reflectometry (PNR) of SL  $n = 5$ , measured at  $T = 5$  K and  $B = 1$  T; and c) the modeled distribution of magnetic moment along the growth direction superimposed on the HRSTEM image.

each layer.<sup>[30]</sup> To visualize the evolution of the possible band alignment at SMO/LMO interfaces a 2D mapping of the O K and Mn  $L_{2,3}$  edges is presented in Figure 3c,d like it was done in refs. [9] and. [31] The results show a significant variation of both edges at the interfaces. A clear broadening of the Mn  $L_3$  peak is observed within each SMO layer. It is also

readily noticeable that the first SMO layer right on the STO substrate for the  $n = 5$  sample has the same Mn  $L_{2,3}$  edge as the other SMO layers (similar broadening). A broadening of the prepeak at the O K edge and an increase of its intensity appears systematically in each SMO layer. Furthermore, the features of hybridized Sr4d-O2p states in the energy range

**Table 1.** Structural characteristics of LSMO films ( $n = 0$ ) and  $(\text{LMO})_{2n}/(\text{SMO})_n$  superlattices.

Sample, $n_{\text{nom}}$ [ $n_{\text{eff}}$ ]	Overall thickness [nm]	Bilayer thickness [nm]	Bilayer number [m]	$C_{\text{av}}$ [nm]	$C_{\text{LMO}}$ [nm] [sim.]	$C_{\text{SMO}}$ [nm] [sim.]	$\text{RMS}_{\text{Int}}$ [nm]	$\text{RMS}_{\text{Sur}}$ [nm]
LSMO1 ( $n = 0$ )	5	—	—	0.384	—	—	—	0.2
LSMO2 ( $n = 0$ )	36.3	—	—	0.385	—	—	—	0.3
1(0.8)	37.5	1.21	32	0.385	—	—	0.3	0.2
2(1.8)	31.00	2.032	16	0.386	0.389	0.379	0.1	0.26
3(2.8)	45.29	4.256	11	0.385	0.390	0.377	0.13	0.15
4 (3.6)	49.67	4.6	11	0.386	0.388	0.378	0.1	0.3
5(4.8) $(\text{LMO}_{14}/\text{SMO}_5)$	71.6	7.26	10	0.387	0.388	0.375	0.1	0.1

536–539 eV within each SMO layers are clearly visible, indicating the absence of significant intermixing or band alignment as the spectrum is identical to that of bulk SMO. On the other hand, we can notice a distinct difference between the LMO/SMO interface and the SMO/LMO interfaces in the O

K edge spectra, correlated to the change discussed above. The SMO/LMO interface has a sharp change of fine structure while this change is smoother in the case of the LMO/SMO interface. This might indicate the presence of charge transfer at the SMO/LMO interface.

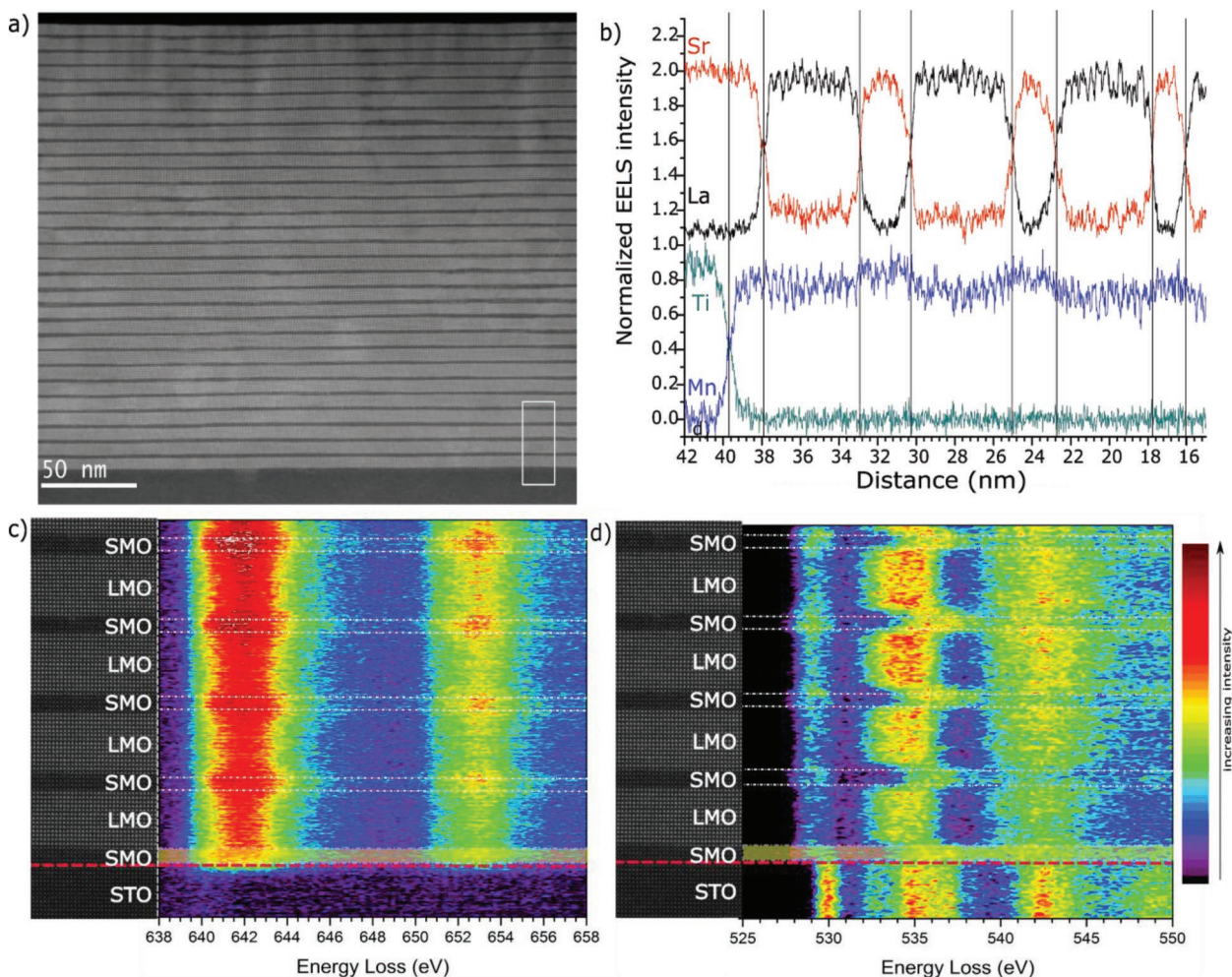


**Figure 3.** a) STEM-HAADF image of the full superlattice with  $n = 5$ , the white rectangle at the bottom right corner represents the region used for EELS measurements; b) compositional profile showing the absence of intermixing and good quality of the superlattice. All profiles are normalized by their maximum; edges used are Sr  $L_{2,3}$ , La  $M_{4,5}$ , Ti  $L_{2,3}$ , and Mn  $L_{2,3}$ . The layer by layer 2D representation of the Mn  $L_{2,3}$  c) and O k d) edge demonstrate the broadening of the Mn  $L_{2,3}$  edge within each SMO layer, and a distinct difference in the electronic structure between the SMO and LMO layers, which is a further sign of the absence of intermixing between the layers.

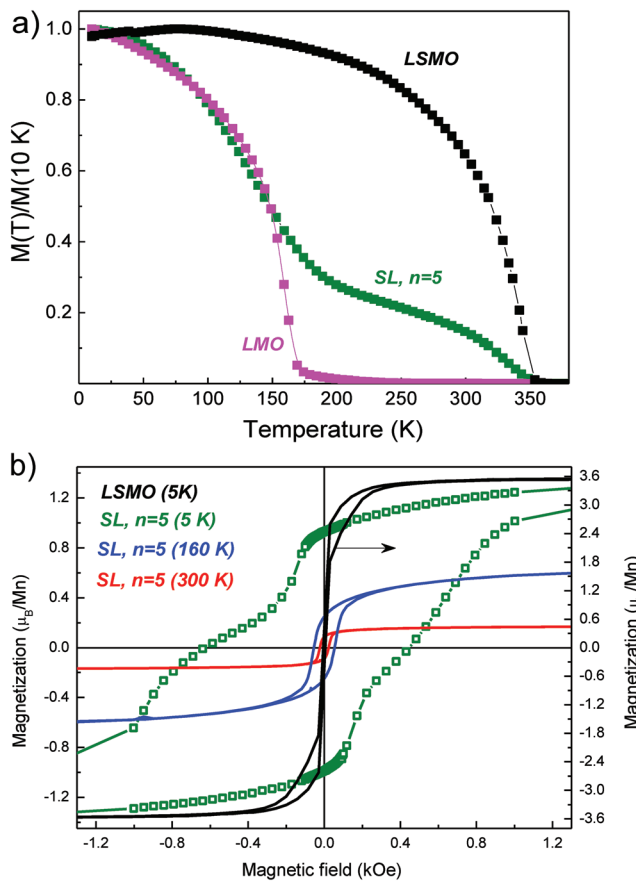


**Figure 4.** a)  $M(T)/M(10 \text{ K})$  dependences reveal FM transitions at  $T_C(\text{LSMO}) = 355 \text{ K}$  and  $T_C(\text{LMO}) = 170 \text{ K}$  and a two-phase behavior for SL with  $n = 5$ ; b)  $M(H)$  field dependences. LSMO at  $T = 5 \text{ K}$  (black curve, right scale) shows low coercive field and homogeneous FM behavior ( $M_{\text{sat}} = 3.6 \mu_B/\text{Mn}$ ). SL with  $n = 5$  demonstrates a reduced saturation magnetization at  $5 \text{ K}$  down to  $M_{\text{sat}} = 1.3 \mu_B/\text{Mn}$  (olive) and a drastic increase of coercive field ( $H_c = 550 \text{ Oe}$ ) as well as an exchange bias ( $H_{\text{EB}} = 100 \text{ Oe}$ ). The high- $T_C$  FM phase is evidenced by the  $M(H)$  curve at  $300 \text{ K}$  ( $M_{\text{sat}} = 0.2 \mu_B/\text{Mn}$ ,  $H_c = 23 \text{ Oe}$ ); at  $T = 160 \text{ K}$  both  $H_c$  and  $M_{\text{sat}}$  show an increase as the low temperature FM phase with  $T_C(\text{LMO}) = 170 \text{ K}$  evolves.

In **Figure 4** we present the temperature- and field-dependent magnetic behavior of the SL with  $n = 5$  in comparison with LSMO and LMO single films grown on STO(001) substrates. The LSMO film ( $n = 0$ ,  $D = 36 \text{ nm}$ ) shows a classic double exchange magnetism<sup>[20,32]</sup> with a ferromagnetic transition at  $T_C = 355 \text{ K}$  (see **Figure 4a**).  $T_C$  was defined<sup>[33]</sup> from the minimum of the function  $\text{TCM} = (1/M)(dM/dT)$ , where “ $M$ ” means magnetization. The LMO film, in contrast to the A-AFM ground state in the bulk,<sup>[20]</sup> shows an FM behavior with  $T_C = 160 \text{ K}$ . The ferromagnetism in LMO epitaxial films is known to be stabilized by strain<sup>[34]</sup> and stoichiometric (or over-stoichiometric) oxygen concentration.<sup>[28]</sup> In our case, likely, a small biaxial tensile strain,  $\epsilon \approx 0.5\%$ , could be provided by the STO(001) substrate (see Table 1) and we assume the absence of oxygen deficiency due to high oxygen partial pressure,  $p_{\text{O}_2} \approx 0.2 \text{ bar}$ , within MAD. The magnetic response of an SMO film with  $d = 40 \text{ nm}$  was hardly measurable (not shown) in agreement with the AFM ground state, stabilized additionally

by strain.<sup>[35]</sup> The magnetic hysteresis loop of a single LSMO film, measured at  $T = 5 \text{ K}$  and shown in **Figure 4b**, confirms an FM behavior with a very low coercive field,  $H_c(\text{LSMO}) = 6 \text{ Oe}$ , and saturation magnetization,  $M_{\text{sat}} = 3.6 \mu_B/\text{Mn}$ , in good agreement with Sr-doping level,  $x \approx 0.33$ .

Remarkably, the  $M(T)$  and  $M(H)$  behavior (see **Figure 4a,b**) in SLs with  $n > 3$  differs drastically from that measured for homogeneous manganite films. For the  $n = 5$  SL one can see two well-separated transitions with  $T_{C1} < T_{C2}$ , marking the low (LTP)- and high-temperature (HTP) FM phases, respectively. Moreover, the significantly decreased saturation magnetization,  $M_{\text{sat}}(5 \text{ K}) \approx 1.5 \mu_B/\text{Mn}$ , the strongly enhanced coercive field,  $H_c = 550 \text{ Oe}$ , and a pronounced exchange bias field,  $H_{\text{EB}} \approx 100 \text{ Oe}$  (see **Figure 4b**) all point out the presence of an AFM phase in the  $n = 5$  SL at low temperatures. The HTP FM phase is evidenced by a distinct  $M(H)$  loop at  $300 \text{ K}$  with  $M_{\text{sat}} = 0.2 \mu_B/\text{Mn}$  and  $H_c = 23 \text{ Oe}$ . At  $T = 160 \text{ K}$  both  $H_c$  and  $M_{\text{sat}}$  show an increase as the low temperature FM phase with  $T_C(\text{LMO}) = 170 \text{ K}$  evolves. Generally, the magnetism in SLs was found to depend crucially on the SMO and LMO thickness (see Figure S9 in the Supporting Information). For very thin SMO ( $n = 1, 2$ ) the magnetic behavior of SLs with high  $T_C = 347–336 \text{ K}$ , large saturation magnetization,  $M_{\text{sat}} = 3.5–3.4 \mu_B/\text{Mn}$ , and low coercive fields,  $H_c(5 \text{ K}) = 8–14 \text{ Oe}$ , agrees well with the LSMO-like FM behavior observed in earlier studies.<sup>[10–16]</sup> In SLs with  $n > 3$  the bulk-like magnetism is progressively suppressed and the progressively developing inhomogeneous AFM/FM behavior (see **Figure 5**) is characterized by: a) the coexistence of LTP- and HTP FM phases; b) the suppression of saturation magnetization; c) the enhanced coercive field, and d) the exchange bias phenomenon. All these data strongly support the claim that there is a boundary around  $n_{\text{cr}} = 2$  which separates a homogeneous FM behavior ( $n \leq 2$ ) from a nonhomogeneous FM/AFM coexistence with LTP and HTP for SLs with  $n \geq 3$ . As one can see in **Figure 5a**)  $T_{C1}$  decreases with increasing the thickness of LMO and approaches a value of  $T_C \approx 160 \text{ K}$  for a single LMO film. Hence, it is reasonably to assign the LTP to an LMO-like FM phase, stabilized by thickness, epitaxy stress, and high  $p_{\text{O}_2}$ . The progressively enhanced AFM behavior for SLs  $n > 3$  (see **Figure 5b**), is related most probably to the SMO layer, which by increasing the thickness acquires its natural AFM character. The HTP for SLs with  $n > 3$  displays an almost thickness independent Curie temperature,  $T_{C2} = 352–358 \text{ K}$ , thus, indicating a behavior typical for emergent interfacial phases.<sup>[1]</sup>

Polarized neutron reflectometry (PNR), measured at  $T = 5 \text{ K}$  and magnetic field,  $B = 1 \text{ T}$ , reveals (see **Figure 2b**) a large superlattice peak originating from the LMO/SMO bilayer. In PNR measurements, the “features” of individual reflectivity curves (e.g., oscillations) are due to the nuclear and magnetic scattering length density (SLD) and thickness of individual layers. Because of the extremely close nuclear SLDs of LMO and SMO ( $34.6 \times 10^{-6}$  and  $33.6 \times 10^{-6} \text{ \AA}^{-1}$ , respectively), almost all contrast in the PNR seen here must stem from the magnetic contrast across the system. Hence, the magnetization across the sample must be unequally distributed between the LMO and SMO layers and this distribution should be highly periodic with each (LMO/SMO) bilayer. For higher temperatures, because of the very weak magnetic moment and low scattering

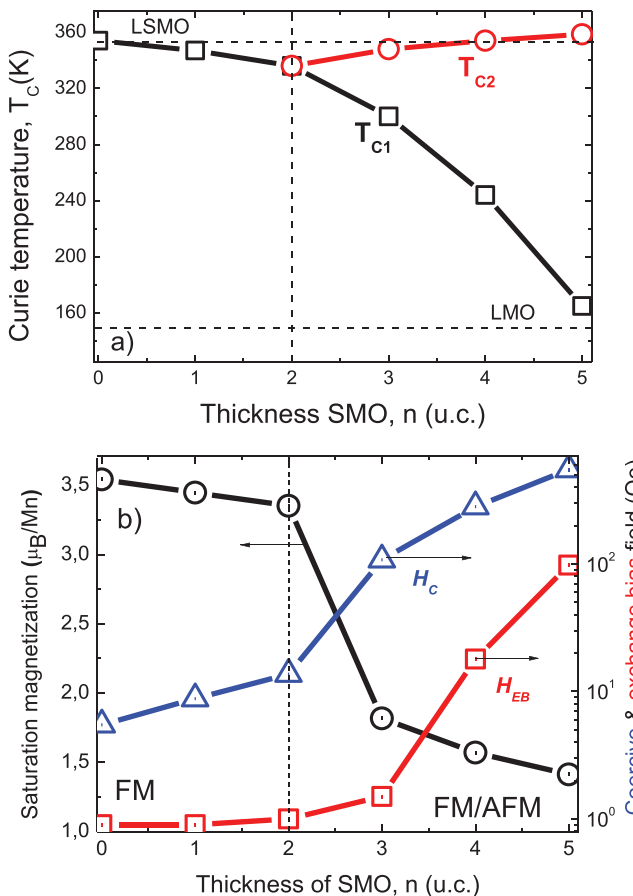


**Figure 5.** a) Curie ( $T_c$ ) and metal–insulator transition ( $T_{MI}$ ) temperatures illustrate the appearance of a high- $T_c$  ferromagnetism and suppression of  $T_{c1}$  and  $T_{MI}$  for  $n > 2$ ; b) Increase of coercive ( $H_c$ ) and appearance of exchange bias ( $H_{EB}$ ) field as well as suppression of saturation magnetization ( $M_{sat}$ ) indicate progressive enhancement of AFM phase for  $n > 2$ . The phase boundary at  $n \approx 2$  separates a homogeneous FM and an FM/AFM phase coexistence in LMO/SMO SLs.

contrast between the LMO and SMO layers, almost featureless PNR patterns were obtained (not shown). In order to fit the low temperature data, each LMO/SMO bilayer was treated with a single nuclear SLD that is an average of the LMO and SMO SLDs. The bilayer was then broken down into seven individual layers, each with a thickness of  $\approx 1$  nm and the magnetic moment within each layer was varied in order to best fit the PNR data. From the PNR data and simulations we deduced that the strongest magnetic moment should be concentrated close to the SMO/LMO interface as shown in Figure 2c) rather than homogeneously distributed within the LMO layer. Remarkably, the first 3 u.c. of the LMO layer (after the SMO) possess almost no magnetic moment, indicating, probably, an AFM or a highly disordered spin state even at  $B = 1$  T. Considering a further increase of magnetic moment within the next 10 u.c. of the LMO (see Figure 2c), a strongly inhomogeneous magnetic state within the LMO can be concluded. The enhancement of the magnetism at the SMO/LMO interface in the MAD grown SLs, being in contrast with the earlier results,<sup>[3,16]</sup> which claimed that enhanced magnetism existed at the LMO/SMO

interface and attributed this behavior to a high interfacial roughness, which is not the case here. The localization of an enhanced moment at the SMO/LMO interface then provides a rational basis that the observed HTP, with  $T_c \approx 360$  K from magnetic measurements, is the origin for this novel phase.

The physical reason of the formation of interfacial HTP in LMO/SMO SLs can be deduced from the in situ growth monitoring by optical ellipsometry, directly superimposed onto the HRTEM HAADF image as shown in Figure 6 (here the delays between SMO and LMO precursor pulses in the  $\Delta(t)$  diagram were removed). This approach is additionally supported by the XRR and XRD data (see Table 1), which agree quantitatively with the nominal and TEM-observed thicknesses of the individual SMO and LMO layers as well as of the whole SL stack. As we have shown above for the reference single LSMO film with thickness  $D = 5$  nm, the linear time dependence of the ellipsometric phase shift angle,  $\Delta$ , allows one to renormalize the time evolution,  $\Delta(t)$ , into a thickness dependence, i.e.,  $\Delta = A^*(v*t) = A^*D$ , for a constant deposition rate,  $v$ . Note that the film thickness,  $D$ , was measured independently by XRR. The obtained “phase shift rate,”  $A_{LSMO} = d\Delta/dD = 0.32^\circ$  per u.c., is almost constant along the growth direction (see Figure 1a) in agreement with the assumed constant electronic density,  $N = 1 - x$ , for a homogeneously doped LSMO film. However, if the electronic properties of the LMO or SMO layers will modify during the SL growth the  $\Delta$  signal will be additionally affected by the “electronic” parameter  $A_n(N, D)$ , which reflects the changes in the charge density,  $N$ , within the thickness,  $D$ , of the layer. Indeed, one can see in Figures 1 and 6, a nonmonotonous  $\Delta(D)$  behavior within SMO layers for SL  $n = 5$ . The first 2 u.c. of SMO display a large initial slope,  $d\Delta/dD = A_n(N) \approx 0.4^\circ$  per u.c., which even exceeds the slope for the following LMO layer,  $\approx 0.31^\circ$  per u.c. This indicates an enhancement of the interfacial electronic density (optical conductivity) in the SMO, which otherwise should be much lower compared to the LMO.<sup>[36]</sup> As the following 3 u.c. of SMO start to grow, the phase shift rate abruptly decreases (Figure 6) and then remains almost constant and small,  $A_n(N, D) \approx 0.1^\circ$  per u.c., in full agreement with the decreased charge density in an electron-poor SMO. The integral taken over one bilayer with thickness,  $\Lambda$ , and normalized to it,  $A_{SL} = \Lambda^{-1} \int A_n(x, D) dD = 0.33\text{--}0.38^\circ$  per u.c., deviates little for different SLs and is close to the value for an individual LSMO film (Figure 1),  $A_{LSMO} = 0.32^\circ$  per u.c. All this supports the idea that the ellipsometric phase shift rate,  $d\Delta/dD$ , probes the charge density/u.c. or the averaged doping level,  $x = n/(m + n)$ , which nominally should be similar in all SLs. The main difference between the single LSMO film ( $n = 0$ ) and SLs with  $n = 1, 2$ , from one side, and SLs with  $n = 3\text{--}5$ , from the other side, is that the charge density in the latter is not homogeneously distributed within the SL. We have simulated the measured  $\Delta(D)$  behavior for SL with  $n = 5$  (for details see Section S8 in the Supporting Information and ref. [37]) by means of a simple optical model, which takes into account the change of optical constants by consecutive growth of very thin artificial layers of LMO and SMO. The values of imaginary and real part of the complex refraction index,  $\eta + i\kappa$ , were calculated from the ellipsometry measurements of LMO and SMO films carried out at  $T = 900$  °C (ref. [38]). One can see that allowing the electron transfer at the SMO/LMO interface by artificial

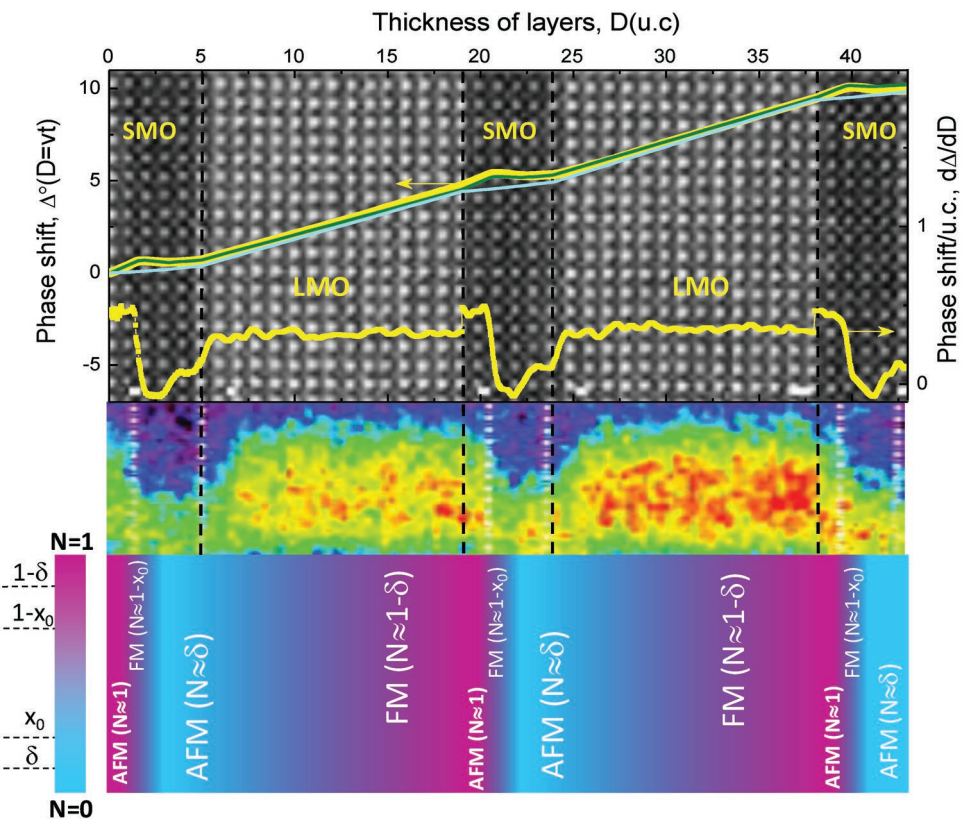


**Figure 6.** Top panel: the evolution of the ellipsometric phase shift (left scale) with the film thickness ( $D = vt$ ) in SL  $n = 5$ , directly superimposed onto the corresponding HAADF HRTEM image. The experimental  $\Delta(D)$  “yellow” curve is well reproduced by the simulated one (“green”) under assumption of an electron transfer within the first 2 u.c. of SMO. The simulated  $\Delta(D)$  behavior in SMO layer without charge transfer (“cyan” curve) does not fit to the measured one. The calculated phase shift/unit cell (“yellow” curve),  $d\Delta/dD$ , represents the evolution of electron density within LMO/SMO layers. Middle panel: the distribution of the O K (d) edge structure close to 535 eV along the growth direction shows the electron-rich (“yellow”) and electron-poor or hole-rich (“blue”) regions within the SMO and LMO layers, respectively. Bottom panel: the modeled distribution of the resulting electron density along the growth direction for SL with  $n = 5$  with HTP and LTP FM phases (“red” regions), separated by two AFM phases: electron-rich (“red”) in SMO and hole-rich (“blue”) in the SMO and LMO.

introducing of 2–3 u.c. of electronically rich LMO (“green” curve in Figure 6, bottom panel) fits nicely the measured  $\Delta(D)$  behavior. Without this assumption the simulated “blue” curve (Figure 6), representing the pure SMO behavior, does not fit the measured data.

A qualitative model of the electron density distribution along the growth direction of an LMO/SMO SL with  $n = 5$  is shown in Figure 6 (bottom panel). Due to the electron transfer across the SMO/LMO interface, the SMO layers close to the interface acquire electrons, becoming quasioptimally doped and ferromagnetic in agreement with the phase diagram of Sr-doped LMO.<sup>[39]</sup> Note, that a driving force for the charge transfer is the polar mismatch as SMO (LMO) possesses a shortage (excess) of electrons, compensated or at least diminished by spreading the electrons into the SMO during growth. Another interface LMO/SMO remains electronically sharp as the same driving force tends to transfer electrons onto the grown surface of LMO to compensate their absence in vacuum. Our interpretation considers mainly the electrostatic mismatch between LMO and SMO, assuming a perfect oxygen stoichiometry and the absence of lattice relaxation effects, i.e., Jahn–Teller and tetragonal distortions. Lattice effects are out of the scope of

this paper, but will be considered in the near future. The formation of oxygen vacancies in SMO and their gradients (flow) into LMO, potentially diminishing the electrostatic LMO/SMO mismatch, is hardly to (dis)prove experimentally. However, the strongest magnetization was registered in SMO (Figure 2) but not in LMO, thus, indicating no oxygen transport into LMO. Moreover, the *in situ* ellipsometry infers (Figure 6) rather low electron density and, thus, no oxygen vacancies at the grown surface of SMO. Generally, we believe formation of oxygen vacancies within MAD seems to be unlikely because of high  $p_{O_2} \approx 0.2$  bar. Our results are in good agreement with the earlier theoretical calculations of Calderon et al.,<sup>[40]</sup> pointing out the excess of  $e_g$  electrons at the surface of an LSMO material, i.e., an electron-rich and LMO-like surface termination. The scale of such an electron transfer, taken from the ellipsometry-thickness evolution in Figure 6, consists of two perovskite cells,  $\lambda_{TF} \approx 2$  u.c. = 0.779 nm, and provides a clear physical reason for the existence of a critical thickness  $n_{cr} = 2$  u.c., which separates a homogeneous LSMO-like FM ground state for  $n \leq 2$  and inhomogeneous LTP/HTP state with FM/AFM coexistence for  $n \geq 3$ .

The obtained length scale of charge transfer fits well to the theoretical considerations on the electronic reconstruction

and spreading of charge within about 2–3 u.c. at the LSMO surface by Calderon et al.<sup>[40]</sup> and at the LaTiO<sub>3</sub>/STO interface by Okamoto and Millis.<sup>[41]</sup> However, in contrast to the experimentally measured 2D metallic LaAlO<sub>3</sub>/STO<sup>2</sup> interface and the theoretically proposed metallicity of LaTiO<sub>3</sub>/STO<sup>[40]</sup> interfaces, the SMO/LMO interfaces in our SLs do not reveal a metallic behavior but rather show an FM insulating ground state (Figure S5 in the Supporting Information), likely, because of a complex FM/AFM interplay on the nm scale. Namely, the observed magnetic decoupling between HTP and LTP, manifested by two distinct coercive forces in  $M(H)$  curves in Figure 4b, can be explained by a spatial separation of the interfacial HTP phase by two AFM layers. The first one, located at the right side from HTP, is composed from the “nonmodified” residual 3 u.c. of SMO layer with a small charge density (see Figure 6), as well as from the neighboring 3 u.c. of an electron-poor (hole-overdoped) LMO because of charge conservation during the electron transfer into the SMO. Note, that the in situ measured  $\Delta(t)$  diagrams (Figure 1) can be viewed as snapshots of charge distribution and cannot display the following reduction of the electron density in the already grown LMO donor layer. This scenario is supported by the PNR data, indicating a strongly reduced moment ( $M = 0$  in Figure 2c) within the 3 u.c. of LMO close to the LMO/SMO interface. Moreover, this is also in line with decreasing of  $T_C$  with increasing LMO thickness in Figure 4: the thicker LMO layer becomes overall less hole-overdoped and more stoichiometric. The second AFM layer, is located at the left side from HTP. It is formed within 1 u.c. of SMO due to an electron overdoping as indicated by a very large ellipsometric phase shift rate,  $A_n(N) = 0.4^\circ$  per u.c., in Figure 6, which even exceeds that of the LMO layer,  $A_n(N) = 0.31^\circ$  per u.c. Finally, the model agrees well with the experimentally obtained distribution of the O K edge structure close to 535 eV (Figure 6, middle panel), also displaying the alternation of electron-rich (“yellow-red”) and electron-poor or hole-rich (“blue”) regions within the SMO and LMO layers, respectively.

### 3. Conclusion

In summary, a new high- $T_C$  interfacial FM phase was found in  $[(\text{LMO})_m/(\text{SMO})_n]_K$  ( $n \geq 3$ ) SLs grown on STO(001) substrates by MAD technique. This emerging phase, being confined within  $\approx 2$  u.c. of SMO, results from a charge transfer across the SMO/LMO interface, indicated by the in situ optical ellipsometry and independently confirmed by the polarized neutron scattering and EELS maps. The emerging high- $T_C$  ferromagnetism, triggered by an  $e_g$ -electron transfer from the LMO(donor) to SMO(acceptor), is caused by a delicate charge balance yielding an optimally electron-doped 2D-SMO without cation disorder. In situ optical ellipsometry provides a powerful tool not only to monitor the thickness of the growing layers, but also to get insight into their electronic properties.

### 4. Experimental Section

**Sample Preparation:**  $[(\text{LMO})_m/(\text{SMO})_n]_K$  SLs with  $n = 1\text{--}5$  u.c. and the number of bilayers,  $K = 10\text{--}30$ , were grown using the MAD technique

on TiO<sub>2</sub>-terminated STO (001) substrates. Commercially available precursors of La-, Sr, and Mn-(acetylacetones) were dissolved in dimethylformamide and sprayed by means of a compressed air onto a heated substrate,  $T_{\text{sub}} \approx 900^\circ\text{C}$ . The precursor volume was controlled with an accuracy,  $V = 0.1 \mu\text{L}$ , (SyrDos liquid dosing units by HiTec Zang GmbH) which corresponds to a layer thickness,  $\delta \approx 0.01$  u.c. The growth rates of LMO and SMO as well as the exact precursor volumes were determined by growing individual LMO and SMO films with a thickness  $d = 5\text{--}20$  nm. As a result, the growth of SLs with layer thickness,  $n = 1\text{--}5$  u.c., at a deposition rate,  $v = 0.06\text{--}0.1 \text{ nm s}^{-1}$ , was achieved by sequential deposition from the separate liquid channels of distinct volumes, corresponding to  $12 \mu\text{L}$  per LMO<sub>u.c.</sub> and  $8 \mu\text{L}$  per SMO<sub>u.c.</sub> After deposition of each LMO and SMO layer the time delay,  $t = 12$  and  $6$  s, respectively, was applied to pump out the remaining aerosols from the MAD chamber.

**Growth Monitoring:** The growth of SLs was monitored in situ by means of a specially developed optical ellipsometry setup of “polarizer-modulator-sample-analyzer” (PMSA) type.<sup>[42]</sup> The complex reflection coefficient,  $\rho = r_p/r_s = \tan \psi \times e^{i\Delta}$ , of a linearly polarized He-Ne laser beam,  $\lambda = 632.8 \text{ nm}$ , with an angle of incidence,  $\theta_B = 62^\circ$ , close to the Brewster angle of STO substrate was measured by a Si photodiode using a lock-in-technique on a fundamental,  $\omega = 50 \text{ kHz}$ , and second harmonic,  $2\omega = 100 \text{ kHz}$ , frequency. The phase shift,  $\Delta$ , between the parallel (p-) and perpendicular (s-) component of the reflected beam, was calculated as  $\Delta = \arctan(I_\omega/I_{2\omega})$  (ref. [42]); here  $I_\omega$  and  $I_{2\omega}$  are the measured intensities at the fundamental and second harmonic frequencies. The ellipsometric signal measured at a Brewster angle of incidence  $\theta_B$  (the p-component of the reflected signal vanishes,  $r_p \approx 0$ ) is known to be extremely sensitive<sup>[42]</sup> to the changes of the film’s optical properties. It is used for the in situ growth monitoring of semiconducting Al<sup>III</sup>B<sup>V</sup> films<sup>[43,44]</sup> by means of metalorganic chemical vapor deposition (MOCVD). Considering the vacuum-free character of the MAD technique, the optical ellipsometry is a unique practical alternative to the reflection high-energy electron diffraction (RHEED) technique, used for the growth control within PLD and MBE vacuum setups, operating at much lower  $p\text{O}_2 < 1 \text{ mbar}$ .

**Structural Characterization:** The layer thicknesses and the crystallographic structure of the grown film samples was studied ex situ by means of XRR and XRD followed by simulations by using the ReMagX program.<sup>[45]</sup> STM (Nanoscope IV) and atomic force (AFM, Innova-Bruker) microscopy were used to characterize the film surface morphology. STEM imaging using HAADF and EELS were performed on a Titan 80–300 microscope equipped with an aberration corrector for the probe forming lens and an electron monochromator yielding an energy resolution of 100 meV with a Gatan Quantum spectrometer. This setup has been used at 300 kV acceleration voltage for imaging with a 20 mrad convergence angle and a collection angle of 40–95 mrad. For spectroscopy, spectrum imaging was performed as a line scan at 120 kV acceleration voltage with an exposure time of 0.25 s pixel<sup>-1</sup> and a dispersion of 0.05 eV pixel<sup>-1</sup> to collect the spectrum at the O K edge (530 eV) and at the Mn L<sub>2,3</sub> edge (640 eV).

**Magnetic Characterization:** Magnetic and resistive measurements were carried out in the temperature range,  $T = 5\text{--}400 \text{ K}$ , for external magnetic fields,  $H = 0\text{--}50 \text{ kOe}$ , by using MPMS (SQUID) and PPMS from “Quantum design,” respectively. PNR was performed at the PLATYPUS time-of-flight reflectometer at the Australian Nuclear Science and Technology Organization (ANSTO).<sup>[46]</sup> During PNR measurements, specular scattering geometry is used to simultaneously probe the nuclear (essentially structural) and magnetic scattering length densities (SLD) across the sample in the out-of-plane direction.<sup>[47]</sup> The reflectivity pattern as a function of scattering vector,  $Q = 4\pi\sin(\theta)/\lambda$ , ( $\lambda$  is neutron wavelength and  $\theta$  is a scattering angle) were modeled to obtain both a profile of the composition and magnetization along the depth of the sample. To obtain magnetic information, reflectivity was measured for two opposite neutron spin polarizations,  $R+$  and  $R-$ , where the difference in the modeled SLDs between the two spin states is proportional to the magnetic SLD of the sample. The PNR study was performed on the  $[(\text{LMO})_{15}/(\text{SMO})_5]_{10}$  SL ( $n = 5$ ), which allows the first superlattice diffraction peak, appearing at  $Q \approx 8.5 \times 10^{-2} \text{ \AA}^{-1}$ , to fall well within the

accessible scattering vector detection range. The sample was field-cooled in 1 T, applied parallel to the neutron spin axis, from 350 to 5 K and was subsequently measured at that field value. Higher temperature measurements were made at 225 and 350 K. PNR data analysis was performed using the software package SIMULREFLEC.<sup>[48]</sup>

## Supporting Information

Supporting information is available

## Acknowledgements

The authors thank EU FP7 Framework (Project IFOX) and DFG (SFB 1073, TP B04, A02, Z02) for the financial support. J.V., K.M.C, and N.G. acknowledge funding through the GOA project "Solarpaint" of the University of Antwerp and from the FWO project G.0044.13N (Charge ordering). The microscope used in this work was partly funded by the Hercules Fund from the Flemish Government. The PNR experiment was funded by the Australian Nuclear Science and Technology Organization (proposal number P3985). F.L. acknowledges financial support from the Swiss National Science Foundation (SNF) via grant No. 200020-172611. The Acknowledgements were updated to reflect additional funding details on May 4, 2020 after initial online publication.

## Conflict of Interest

The authors declare no conflict of interest.

## Keywords

charge transfer, interfaces, interfacial ferromagnetism, oxide superlattices

- [1] H. Y. Hwang, Y. Iwasa, M. Kawasaki, B. Keimer, N. Nagaosa, Y. Tokura, *Nat. Mater.* **2012**, *11*, 103.
- [2] A. Ohtomo, H. Y. Hwang, *Nature* **2004**, *427*, 423.
- [3] A. Bhattacharya, S. J. May, S. G. E. te Velthuis, M. Warusawithana, X. Zhai, B. Jiang, Z.-M. Zuo, M. R. Fitzsimmons, S. D. Bader, J. N. Eckstein, *Phys. Rev. Lett.* **2008**, *100*, 257203.
- [4] K. S. Takahashi, M. Kawasaki, Y. Tokura, *Appl. Phys. Lett.* **2001**, *79*, 1324.
- [5] A. Gozar, G. Logvenov, L. Fitting Kourkoutis, A. T. Bollinger, L. A. Giannuzzi, D. A. Muller, I. Bozovic, *Nature* **2008**, *455*, 782.
- [6] P. F. Chen, B. B. Chen, X. L. Tan, H. R. Xu, X. F. Xuan, Z. Guo, F. Jin, W. B. Wu, *Appl. Phys. Lett.* **2013**, *103*, 262402.
- [7] K. Gehrke, V. Moshnyaga, K. Samwer, *Phys. Rev. B* **2010**, *82*, 113101.
- [8] Y. Z. Chen, F. Trier, R. J. Green, N. Gauquelin, R. Egoavil, D. V. Christensen, G. Koster, M. Huijben, N. Bovet, S. Macke, F. He, R. Sutarto, N. H. Andersen, J. A. Sulpizio, M. Honig, G. E. D. K. Prawiroatmodjo, T. S. Jespersen, S. Linderoth, S. Ilani, J. Verbeeck, G. Van Tendeloo, G. Rijnders, G. A. Sawatzky, N. Pryds, *Nat. Mater.* **2015**, *14*, 801.
- [9] A. Belenchuk, O. Shapoval, V. Roddatis, V. Bruchmann-Bamberg, K. Samwer, V. Moshnyaga, *Appl. Phys. Lett.* **2016**, *109*, 232405.
- [10] P. A. Salvador, A.-M. Haghiri-Gosnet, B. Mercey, M. Hervieu, B. Raveau, *Appl. Phys. Lett.* **1999**, *75*, 2638.
- [11] T. Koida, M. Lippmaa, T. Fukumura, K. Itaka, Y. Matsumoto, M. Kawasaki, H. Koinuma, *Phys. Rev. B* **2002**, *66*, 144418.
- [12] S. Smadici, P. Abbamonte, A. Bhattacharya, X. Zhai, B. Jiang, A. Rusydi, J. N. Eckstein, S. D. Bader, J.-M. Zuo, *Phys. Rev. Lett.* **2007**, *99*, 196404.
- [13] C. Aruta, C. Adamo, A. Galdi, P. Orgiani, V. Bisogni, N. B. Brookes, J. C. Cezar, P. Thakur, C. A. Perroni, G. De Filippis, V. Cataudella, D. G. Schlom, L. Maritato, G. Ghiringhelli, *Phys. Rev. B* **2009**, *80*, 140405(R).
- [14] G. Wang, R. Du, D. Wu, A. Li, *J. Appl. Phys.* **2012**, *112*, 103917.
- [15] H. Yamada, M. Kawasaki, T. Lottermoser, T. Arima, Y. Tokura, *Appl. Phys. Lett.* **2006**, *89*, 052506.
- [16] S. J. May, A. B. Shah, S. G. E. te Velthuis, M. R. Fitzsimmons, J. M. Zuo, X. Zhai, J. N. Eckstein, S. D. Bader, A. Bhattacharya, *Phys. Rev. B* **2008**, *77*, 174409.
- [17] O. Chmaissem, B. Dabrowski, S. Kolesnik, J. Mais, D. E. Brown, R. Kruk, P. Prior, B. Pyles, J. D. Jorgensen, *Phys. Rev. B* **2001**, *64*, 134412.
- [18] T. Takeda, S. Ohara, *J. Phys. Soc. Jpn.* **1974**, *37*, 275.
- [19] A. Urushibara, Y. Moritomo, Y. Arima, A. Asamitsu, Y. Tokura, G. Kido, N. Furukawa, *Phys. Rev. B* **1995**, *51*, 14103.
- [20] M. Huijben, Y. Liu, H. Boschker, V. Lauter, R. Egoavil, J. Verbeeck, S. G. T. E. Velthuis, G. Rijnders, G. Koster, *Adv. Mater. Interfaces* **2015**, *2*, 1400416.
- [21] A. Ohtomo, D. A. Muller, J. L. Grazul, H. Y. Hwang, *Nature* **2002**, *419*, 378.
- [22] N. Nakagawa, H. Y. Hwang, D. A. Muller, *Nat. Mater.* **2011**, *10*, 189.
- [23] E. Benckiser, M. W. Haverkort, S. Brück, E. Goering, E. S. Macke, A. Frañó, X. Yang, O. K. Andersen, G. Cristiani, H.-U. Habermeier, A. V. Borís, I. Zegkinoglou, P. Wochner, H.-J. Kim, V. Hinkov, B. Keimer, *Nat. Mater.* **2011**, *10*, 189.
- [24] A. Tebano, C. Aruta, S. Sanna, P. G. Medaglia, G. Balestrino, A. A. Sidorenko, R. De Renzi, G. Ghiringhelli, L. Braicovich, V. Bisogni, N. B. Brookes, *Phys. Rev. Lett.* **2008**, *100*, 137401.
- [25] V. Moshnyaga, I. Khoroshun, A. Sidorenko, P. A. Petrenko, A. Weidinger, M. Zeitler, B. Rauschenbach, R. Tidecks, K. Samwer, *Appl. Phys. Lett.* **1999**, *74*, 2842.
- [26] M. Jungbauer, S. Hühn, R. Egoavil, H. Tan, J. Verbeeck, G. Van Tendeloo, V. Moshnyaga, *Appl. Phys. Lett.* **2014**, *105*, 251603.
- [27] O. Shapoval, S. Hühn, J. Verbeeck, M. Jungbauer, A. Belenchuk, V. Moshnyaga, *J. Appl. Phys.* **2013**, *113*, 17C711.
- [28] M. Yahia, H. Batis, *Eur. J. Inorg. Chem.* **2003**, *2003*, 2486.
- [29] A. Rosenauer, Th. Mehrtens, K. Müller, K. Gries, M. Schowalter, P. V. Satyam, S. Bley, Ch. Tessarek, D. Hommel, K. Sebald, M. Seyfried, J. Gutowski, A. Avramescu, K. Engl, S. Lutgen, *Ultramicroscopy* **2011**, *111*, 1316.
- [30] A. Galdi, C. Aruta, P. Orgiani, C. Adamo, V. Bisogni, N. B. Brookes, G. Ghiringhelli, D. G. Schlom, P. Thakur, L. Maritato, *Phys. Rev. B* **2012**, *85*, 125129.
- [31] N. Gauquelin, D. G. Hawthorn, G. A. Sawatzky, R. X. Liang, D. A. Bonn, W. N. Hardy, G. Botton, *Nat. Commun.* **2014**, *5*, 4275.
- [32] *Colossal Magnetoresistive Oxides* (Ed.: Y. Tokura), Advances in Condensed Matter Science, Vol. 2, Gordon and Breach Science Publishers, Amsterdam, The Netherlands **2000**.
- [33] V. Moshnyaga, L. Sudheendra, O. I. Lebedev, S. A. Köster, K. Gehrke, O. Shapoval, A. Belenchuk, B. Damaschke, G. Van Tendeloo, K. Samwer, *Phys. Rev. Lett.* **2006**, *97*, 107725.
- [34] J. Roqueta, A. Pomar, L. Balcells, C. Frontera, S. Valencia, R. Abrudan, B. Bozzo, Z. Konstantinović, J. Santiso, B. Martínez, *Cryst. Growth Des.* **2015**, *15*, 5332.
- [35] Z. Fang, I. V. Solovyev, K. Terakura, *Phys. Rev. Lett.* **2000**, *84*, 3169.

- [36] J. H. Jung, K. H. Kim, T. W. Noh, E. J. Choi, J. Yu, *Phys. Rev. B* **1998**, 57, R11043.
- [37] F. Lyzwa, P. Marsik, V. Roddatis, C. Bernhard, M. Jungbauer, V. Moshnyaga, *J. Phys. D: Appl. Phys.* **2018**, 51, 125306.
- [38] M. Jungbauer, *Dissertation Georg-August-Universität Göttingen*, **2016**
- [39] J. Hemberger, A. Krimmel, T. Kurz, H.-A. Krug von Nidda, V. Y. Ivanov, A. A. Mukhin, A. M. Balbashov, A. Loidl, *Phys. Rev. B* **2002**, 66, 094410.
- [40] M. Calderon, L. Brey, F. Guinea, *Phys. Rev. B* **1999**, 60, 6698.
- [41] S. Okamoto, A. J. Millis, *Nature* **2004**, 428, 630.
- [42] H. Fujiwara, *Spectroscopic Ellipsometry Principles and Applications*, John Wiley & Sons, Ltd., The Atrium, Chichester, UK **2007**.
- [43] J.-T. Zettler, T. Wethkamp, M. Zorn, M. Pristovsek, C. Meyne, K. Ploska, W. Richter, *Appl. Phys. Lett.* **1995**, 67, 3783.
- [44] J.-S. Lee, Y. Masumoto, *J. Cryst. Growth* **2000**, 221, 111.
- [45] S. Macke, A. Radi, J. E. Hamann-Borrero, A. Verna, M. Bluschke, S. Brück, E. Goering, R. Sutarto, F. He, G. Cristiani, M. Wu, E. Benckiser, H.-U. Habermeier, G. Logvenov, N. Gauquelin, G. A. Botton, A. P. Kajdos, S. Stemmer, G. A. Sawatzky, M. W. Haverkort, B. Keimer, V. Hinkov, *Adv. Mater.* **2014**, 26, 6554.
- [46] a) T. Saerbeck, F. Klose, A. P. le Brun, J. Füzi, A. Brule, A. Nelson, S. A. Holt, M. James, *Rev. Sci. Instrum.* **2012**, 83, 081301; b) M. James, A. Nelson, S. Holt, T. Saerbeck, W. Hamilton, F. Klose, *Nucl. Instrum. Methods Phys. Res., Sect. A* **2011**, 632, 112.
- [47] a) J. F. Ankner, G. P. Felcher, *J. Magn. Magn. Mater.* **1999**, 200, 741; b) M. R. Fitzsimmons, C. Majkrzak, *Modern Techniques for Characterizing Magnetic Materials*, Springer, New York **2005**, pp. 107–155, Ch. 3.
- [48] SimulReflec, Copyright © Lab. Léon Brillouin CEA/SNRS UMR12, <http://wwwllb.cea.fr/prism/programs/simulreflec/simulreflec.html> (accessed: January 2003).